Distinguishing and Quantifying Reversible/Irreversible Lithium in Practical Lithium Metal Batteries

Wei Deng
Ningbo Institute of Materials Technology & Engineering, Chinese Academy of Sciences
Xue Yin
Ningbo Institute of Materials Technology & Engineering, Chinese Academy of Sciences
Wurigumula Bao
University of California, San Diego
Xufeng Zhou
Ningbo Institute of Materials Technology & Engineering, Chinese Academy of Sciences
Zhiyuan Hu
Ningbo Institute of Materials Technology & Engineering, Chinese Academy of Sciences
Bangyi He
Ningbo Institute of Materials Technology & Engineering, Chinese Academy of Sciences
Bao Qiu
Ningbo Institute of Materials Technology & Engineering https://orcid.org/0000-0002-7505-6135
Ying Shirley Meng (shirleymeng@ucsd.edu)
University of California, San Diego https://orcid.org/0000-0001-8936-8845
Zhaoping Liu
Ningbo Institute of Materials Technology and Engineering Chinese Academy of Sciences
https://orcid.org/0000-0003-1770-4605

Article

Keywords: quantitative analytical method, reversible lithium, irreversible lithium, lithium metal anode, practical lithium metal batteries

Posted Date: February 1st, 2022

DOI: https://doi.org/10.21203/rs.3.rs-1308594/v1

Version of Record: A version of this preprint was published at Nature Energy on September 29th, 2022. See the published version at https://doi.org/10.1038/s41560-022-01120-8.

Distinguishing and Quantifying Reversible/Irreversible Lithium in Practical Lithium Metal Batteries

Wei Deng [a, #], *Xue Yin* [a, #], *Wurigumula Bao* [c, #], *Xufeng Zhou* [*, a, b], *Zhiyuan Hu* [a], *Bangyi He* [a], *Bao Qiu* [a, b], *Ying Shirley Meng* [*, c, d, e], *and Zhaoping Liu* [*, a, b]

a Advanced Li-ion Battery Engineering Laboratory of Zhejiang Province, Key Laboratory of Graphene Technologies and Applications of Zhejiang Province, and CAS Engineering Laboratory for Graphene, Ningbo Institute of Materials Technology & Engineering, Chinese Academy of Sciences, Zhejiang 315201, P. R. China

b Center of Materials Science and Optoelectronics Engineering, University of Chinese Academy of Sciences, Beijing 100049, P. R. China

c Department of NanoEngineering, University of California, San Diego, La Jolla, CA 92093, USA

d Materials Science and Engineering, University of California, San Diego, La Jolla, CA 92093, USA

e Pritzker School of Molecular Engineering, University of Chicago, Chicago, IL 60637

# These authors contribute equally to this work.

* Corresponding authors. Tel./Fax: +86-574-8668-5096.

E-mail address: zhouxf@nimte.ac.cn, shirleymeng@uchicago.edu, liuzp@nimte.ac.cn

Keywords: quantitative analytical method, reversible lithium, irreversible lithium, lithium metal anode, practical lithium metal batteries

Abstract:

Practical lithium metal batteries have been researched worldwide, but due to excessive "Li reservoir" in the anode, quantification of the authentic reversibility of practical cells remains unresolved. Quantitative method for assessing the reversibility and irreversibility of Li anode is thereby essentially needed. Here we propose an index system composed of several quantitative parameters to evaluate the reversibility of practical lithium metal batteries. Mathematical relationships between these parameters and cycle number are successfully established based on the mass of active and inactive Li in the cycled Li anode. By establishing a novel and universal analytical method, mass of active Li can be quantitatively distinguished from the inactive one of cycled lithium metal anode in Ah-level pouch cells. Through fitting quantified data of active and inactive Li under different cycles, values of parameters representing for the reversibility and irreversibility of Li are quantitatively decoupled. The quantitative analysis method presented in this work provides new criteria to accurately assess practical lithium metal batteries for more reliable degradation analysis and failure prediction.

Currently, both academic and industrial attentions are focusing on practical lithium metal batteries (LMBs) with energy density beyond 500 Wh/kg.[1-4] But how to distinguish and separate reversible Li from the irreversible one in the cycled lithium metal anode (LMA) for accurate evaluation and quantification of the authentic reversibility of practical LMBs still remains a big challenge.[5,6] For anode-free cells without LMA, the irreversible capacity loss can be easily identified by the Coulombic inefficiency of the cell (CiE_{cell}), and the cycling performance truly reflects cell degradation (Supplementary Fig. 1a).[7,8] In contrast, in LMBs, LMA as "Li reservoir" will continuously compensate for the loss of lithium originating from the cathode, therefore the CiE_{cell} does not precisely reflect the real Li loss during cycling.[9-12] In fact, degradation of LMBs is dominantly governed by LMA at present due to the much worse electrochemical reversibility of LMA than that of the cathode.[13-15] Therefore, quantitative parameters reflecting the authentic reversibility and irreversibility of LMA should be established as criteria to objectively assess the degradation behavior of LMBs for better battery design and failure prediction.

It is well known that the irreversible Li (also known as dead Li)in cycled LMA arises from the formation of (electro)chemically formed Li^+ compounds in the solid electrolyte interphase (SEI Li^+) and electrically isolated unreacted metallic Li (inactive Li).[16,17] The continuous formation and agglomeration of such ineluctable "dead Li" upon cycling will gradually accelerate the loss of active Li in LMA as they block the transportation of electrons and Li-ions.[18,19] The ever-changing irreversible loss of Li in LMA ($IRL_{Li,n}$, n corresponds to the cycle number) during cycling can be mathematically expressed based on two parts (Supplementary Fig. 1b), namely the intrinsic Li loss of the pristine LMA ($IRL_{Li,0}$) which is determined by the specific parameters and working conditions of LMBs, and the cycle-number-dependent incremental part which reflects the cumulative effects of the "dead Li" formed within the (n-1) cycles on the irreversible Li loss at the n^{th} cycle . Determination of $IRL_{Li,0}$ and the related incremental part offers the criteria to evaluate and understand the degradation behavior of LMA hidden beneath the apparent CiEs for practical LMBs in a quantitative way. However,

both cannot be directly characterized by simply calculating the total charge flows. As cycled LMA is composed of reversible Li (termed as the active Li) and SEI encapsulated inactive Li (**Figure 1a)**, quantifying active Li and inactive Li in LMA as a prerequisite to decouple reversible Li from the irreversible one makes the determination of two parts possible.[8,11,17,20-24] However, there are still two obstacles to be surmounted to identify them through quantitative chemical analysis. One is how to separate active and inactive Li for independent identification of these species. Although inactive Li was quantified in anode-free coin cells by *in situ* nuclear magnetic resonance[20,21,25-27] and hydrogen titration gas chromatography[17,28], these methods can't distinguish active Li from inactive ones in cycled LMA due to their identical metallic nature.[29] The other issue is how to establish a mathematical relationship that can be used to determine the inherent Li loss and the cycle-number-dependent incremental part from the quantitative analysis results.

Herein we report a novel and universal chemical analytical methodology to quantitatively distinguish the active Li from the inactive one in cycled LMAs in Ah-level LMB pouch cells. Biphenyl/THF solution is employed to dissolve the active Li through complexation but to preserve the completeness of SEI that encapsulates the inactive Li. The as-separated active and inactive Li can be independently quantified by atomic emission spectrometry and gas chromatography, respectively. Furthermore, by introducing an exponential function of cycle number to describe the incremental effect of "dead Li", values of $IRL_{Li,0}$ and the incremental coefficient are decoupled and identified through fitting quantified results of active and inactive Li, which can be employed to analyze the authentic reversibility of LMA in practical LMBs. The variations of $IRL_{Li,n}$ suggest that high stack pressure suppresses inherent Li loss by minimizing the cracking possibility of SEI, and agglomeration of "dead Li" drives dendritic Li plating for more inactive Li. And the inherent Li loss is mainly governed by the electrolyte, charging rates and stack pressures rather than the kinds of cathodes. By using this quantitative analytical method, the blindfold for the compositional and structural evolution of LMA beneath qualitative morphology characterizations can be

uncovered. Quantification of reversible/irreversible Li provides a variable-independent and quantifiable criterion to reflect the magnitude of effects from different variables in LMBs, including external variables (stack pressures, rates, charge voltages, temperatures, etc.) and internal variables (cathodes, anodes, binders, etc.), which can make a significant contribution to better and more efficient LMB cell design.

Mathematical hypothesis

For conventional lithium-ion batteries, the capacity retention after n cycles equals to $(CE_{cell})^n$ owing to nearly unchanged value of the Coulombic efficiency of the cell.[30] In contrast, the $CiE_{cell,n}$ of anode-free cells, which corresponds to $IRL_{Li,n}$, changes along with the cycle number. **Figure 1b** confirms the gradual increase of $CiE_{cell,n}$ of a 0.5 Ah anode-free pouch cell when cycling. Fitting result demonstrates that the proportion of the irreversible Li loss in each cycle is a time-variable exponential function closely related to the cycle number (n). In other words, "dead Li" formed in former cycles will bring accumulative effects to the proliferation of "dead Li" in the latter cycles.[31] Mathematically, the ever-changing $IRL_{Li,n}$ can be expressed in Equation 1 as the inherent irreversibility of LMA ($IRL_{Li,0}$) multiplied by an exponential function of Euler's number with variables of the cycle number (n) and the incremental coefficient (K).

$$IRL_{Li,n} = IRL_{Li,0} * e^{K*n} \quad (1)$$

The same mathematical expression can be applied to understand the irreversibility of LMAs, but sufficient "Li reservoir" of LMA determines that the total irreversible Li loss after a certain cycle number in LMB follows a mathematical addition relationship. The percentage of active Li and cycle number (n) are in a good linear relationship under impeccable conditions with $IRL_{Li,0}$ as the slope as expressed in Equation 2 (Supplementary Fig. 2, details in **Methods**), where C and [N/P] are representative for the areal capacity of the cathode and N/P ratio of the cell, respectively.[10]

$$[active\ Li]\% = 1 - \left(\frac{1}{\left[\frac{N}{P}\right]}\right) * IRL_{Li,0} * n \quad (2)$$

Actually, the authentic $IRL_{Li,n}$ in each cycle deviates from $IRL_{Li,0}$ gradually upon cycling owing to the continuous agglomeration of "dead Li". Thereby, an incremental coefficient (termed as K_{IRL}) with a definition as a correction factor to describe the cycle number dependent incremental irreversibility to $IRL_{Li,0}$ is introduced by using the exponential form based on Euler's number. Its physical meaning can be understood as the joint influences from the inherent irreversibility of LMA and the accumulated parasitic effects from "dead Li" on the deteriorating Li stripping/plating behavior. Interestingly, the accumulative CiE_{cell} from anode-free pouch cell (Supplementary Fig. 1d) shows the same conclusion. Based on this hypothesis, the relationship between $IRL_{Li,0}$, K_{IRL}, [active Li]% and n in practical LMBs is expressed in Equation 3 (mathematical illustration in **Figure 1c**, details in **Methods**).

$$[active\ Li]\% = 1 - \left(\frac{1}{\left[\frac{N}{P}\right]}\right) * IRL_{Li,0} * \frac{e^{K_{IRL}*n}}{K_{IRL}} \quad 3$$

More specifically, $IRL_{Li,n}$ of LMB can be divided into two parts, $IRL_{inactive\ Li,n}$ and $IRL_{SEI,n}$ (**Figure 1d**), which are representative for inactive Li and Li species in SEI, respectively. Similarly, the relationship correlated to inactive Li is expressed as Equation 4 (details in **Methods**), which can be used to calculate the value of $IRL_{inactive\ Li,0}$. However, at present, quantification of the reversible part of Li plating/stripping ($R_{Li,n}$) for LMBs have rarely been reported before.[9] Actually, acquiring values of $R_{Li,0}$ is quite important for assessing the inherent reversibility of a specific LMB. Fortunately, the irreversible Li loss of the cathode is directly related to the average CE_{cell} (as expressed in Equation 11 and 12), thus by knowing values of $IRL_{Li,0}$, $IRL_{inactive\ Li,0}$ and $CE_{cell,\ average}$, $R_{Li,0}$ and $IRL_{SEI,0}$ can be decoupled from CE_{cell} by using Equation 5.

$$[inactive\ Li]\% = \left(\frac{1}{\left[\frac{N}{P}\right]}\right) * IRL_{inactive\ Li,0} * \frac{e^{K_{inactive}*n}}{K_{inactive}} \quad 4$$

$$CE_{cell,average} = R_{Li,0} + IRL_{SEI,0} + IRL_{inactive\ Li,0} \quad 5$$

Based on the above mathematical model, through quantitative determination of active and inactive Li in LMA after cycling (see the next section for details), it is possible to establish an index system composed of several key parameters such as $R_{Li,0}$, $IRL_{Li,0}$,

$IRL_{inactive\ Li,0}$, etc. The definitions for these key parameters are listed in **Table 1**. This index system can be used to quantitatively describe the authentic reversibility and irreversibility of a specific LMB, thus, to scientifically evaluate the effects of key materials, cell parameters and testing protocols on the performance of practical LMBs. Assuming no capacity loss in the cathode, failure prediction of LMBs based on ideal (no accumulative effects) and calibrated (considering agglomeration of "dead Li") conditions are shown in **Figure 1e** to demonstrate the significance of $R_{Li,0}$ and K_{IRL}. With the same value of $R_{Li,0}$, the lifetime of the cell is largely shortened when the cumulative effects from "dead Li" (*K*) is taken into consideration. The calibrated lifetime is much closer to the reality of practical LMBs, demonstrating the validity of this mathematical hypothesis. When $R_{Li,0}$ is increased along with decreasing of K_{IRL}, the reversibility of LMB is evidently improved to deliver hundreds even thousands of cycles. A very small increment in $R_{Li,0}$ and/or decrement in K_{IRL} will cause huge differences in the cyclic stability of the cells. The requirements for $R_{Li,0}$ and K_{IRL} to reach specific cycle numbers under certain conditions are simulated in **Figure 1f**, which can be used for lifetime prediction when knowing the specific values.[32] The above predictions are also consistent with the data published by the Battery500 Consortium. As previously mentioned, CE cannot be directly used to predict the cycle life. Either the SEI growth or accumulation of dead Li should be considered as the build-up effect for the degradation of the LMB.[33] Moreover, in the recently published results with optimized N/P ratio and electrolyte system, the LMB's cycle was extended to more than 600 cycles without the sudden drop, indicating that the well-controlled LMB could demonstrate a *K* value even smaller than 0.005 (orange line in Figure 1e).[12]

Methodology for quantifying active and inactive Li

Active Li, inactive Li and Li composites (from electrolyte or electrodes) in SEI are three major components in cycled LMA (**Figure 2a)**. As active and inactive Li are both metallic Li in terms of their composition, the only difference between them is that inactive Li is the SEI-encapsulated particles.[34] Although bulk Li foil is also covered by

SEI, punching LMAs to small pieces in an Ar-filled glove box for quantitative analysis will expose fresh surface of bulk Li without SEI coverage. Considering the high chemical stability of SEI in organic solvents,[35,36] it is possible to convert active Li to Li-ions by organic solvent[37] without dissolving SEI-protected inactive Li. Herein, hybrids of biphenyl and tetrahydrofuran (THF) are used as such selective solvents. But the stability of SEI (originated from carbonate-based electrolyte in this work) in biphenyl/THF should be verified in advance. First, main inorganic salts (Li_2CO_3, LiF and LiOH) in SEI are verified to be insoluble in biphenyl/THF (Supplementary Table 2). Second, lithium ethylene dicarbonate (LEDC), lithium methyl carbonate (LMC) and lithium ethylene mono-carbonate (LEMC) are the main organic components of ethylene carbonate (EC)/ethyl methyl carbonate (EMC)-derived SEI, and LEDC was reported to be directly synthesized from the chemical reaction between EC and lithium−naphthalenide.[35,36] Both aspects suggest the stability of the inorganic and organic components in SEI against biphenyl/THF and Li-biphenyl/THF. To directly confirm the stability of "dead Li" in (Li-)biphenyl/THF, bare Li foil and anodes from anode-free pouch cells (Supplementary Fig. 5) and LMBs after cycling were immersed in biphenyl/THF. **Figure 2b-d** show that after 48 h of immersion at 25 ℃, no evident color change of the solution containing only "dead Li" on Cu foil (fully stripped anode from anode-free cells) is observed, which is significantly different from the dark color of the solution containing either bare Li or cycled LMA, suggesting high chemical stability of SEI. The digital photographs (Supplementary Fig. 6) and inductively coupled plasma-atomic emission spectrometer (ICP-AES) results (Supplementary Table 3) for the supernatants in **Figure 2b-d** also demonstrate insolubility of SEI in (Li-)biphenyl/THF.

Detailed procedures for separating active and inactive Li are shown in **Figure 2e-g**. Active Li in cycled LMAs was firstly dissolved in biphenyl/THF (6.0 *wt.*% of biphenyl), and its content was quantified by ICP-AES (termed as Li-ion atomic emission spectrometer titration, Li-AEST). Residual inactive Li encapsulated by SEI was then reacted with deionized water. Hydrogen as the reaction product was collected and

quickly injected to gas chromatography (GC) for quantifying the content of inactive Li (termed as hydrogen gas chromatography titration, H_2-GCT). The accuracy and sensitivity of Li-AEST and H_2-GCT were measured before quantitative analysis. As shown in **Figure 2h**, theoretical Li concentrations of standard biphenyl/THF solutions prepared by fully dissolving Li foils with pre-designed masses (Supplementary Fig. 7 and Table 4) are linearly related to the measured concentrations from ICP-AES results, with goodness of fit approaching 1 (R^2=0.99817) and detection limitation down to 10^{-2} mg. To eliminate the interference of additional gases (CO_2, CH_4, C_2H_4, C_2H_6) from the reaction between SEI and water (Supplementary Fig. 8-9 and Table S5) during H_2-GCT measurement, modified method for quantifying hydrogen was proposed by taking argon as the calibration component (detailed descriptions in **Methods**). In **Figure 2i**, the baseline of H_2-GCT shows good linear relationship between the masses of pure Li and the peak area ratios of hydrogen to argon, with R^2=0.99346 and detection limit of 10^{-2} mg. All these results confirm the accuracy of the analytical method we proposed in this work, guaranteeing quantitative and accurate analysis of active and inactive Li in cycled LMA.

Quantifying proportions of reversibility and irreversibility of Li anode

To validate the efficacy of the methodology proposed in this work on practical LMBs, three identical 0.5 Ah Li/NCM811 pouch cells operated under different stack pressures (100/400/800 kPa) were subjected to quantitative analysis. It is well acknowledged that external pressure can significantly affect the reversibility of Li stripping/plating[7,38], but the cycling performance (**Figure 3a**), including the capacity retention (~95% after 50 cycles) and the average CE_{cell} (99.90%), are almost identical for all three cells within 50 cycles, owing to the continuous compensation to the irreversible Li loss from excess metallic Li in the original LMA. By applying the quantitative methodology, the hidden reversibility of LMAs under different pressures can be truly distinguished. Although the capacities of three cells almost overlap within the initial 50 cycles, the mass of active and inactive Li acquired by quantitative measurement at the same cycle number

differs apparently among three cells. It is observed that the amount of active Li increases along with increasing stack pressure from the statistical perspective (**Figure 3c**). Meanwhile, the mass of inactive Li complies with the opposite trend; the formation rate of inactive Li at 100 kPa is the highest among them (**Figure 3d**). The experimental data were then fitted according to Equation 3 and 4, respectively, to acquire the set of key parameters (K_{IRL}, $R_{Li,0}$, $IRL_{inactive\ Li,0}$, $IRL_{SEI,0}$ and the average Li loss of the cathode) that describe the reversibility of LMB under certain conditions. Detailed values of each parameter are listed in Supplementary Table 11. It is noted that the fitting curves are conformal with the measured data, which indicates the validity of the mathematical hypothesis proposed in this work.

As shown in **Figure 3e and f**, increasing stack pressure helps to improve $R_{Li,0}$ from 99.22% at 100 kPa to 99.44% at 800 kPa, while the proportion of $IRL_{SEI,0}$ is reduced from 0.27% to 0.14% as the more flattened morphology of electrochemically plated Li at higher pressure reduces the cracking possibility of SEI.[28,39-42] Interestingly, the proportions of $IRL_{inactive\ Li,0}$ and $IRL_{SEI,0}$ for Li/Li-rich layer oxide cathode (LR-NCM) pouch cells (Supplementary Fig. 10) are almost identical to those of Li/NCM811 cells under the same conditions of 100 kPa and C/5, suggesting the inherent irreversible Li loss is mainly governed by the electrolyte, stack pressure and charging/discharging rates rather than the cathodes. Raising stack pressure also decreases K_{IRL} from 0.01966@100 kPa to 0.01809@400 kPa by densifying the "dead Li" layer. The higher K_{IRL} (0.02931) of Li/LR-NCM cells comparing with that of Li/NCM811 cells is probably caused by the larger Li loss of the LR-NCM cathode with higher areal capacity and higher cut-off voltage (4.6 V). Theoretically, K_{IRL} of Li/NCM811 cells under 800 kPa should be lower than that under 100 or 400 kPa according to the definitions. The anomalously high K_{IRL} at 800 kPa is speculated to be caused by some unnoticed problems during cell assembly or testing procedures. But this abnormal result just shows the high accuracy of this method for judging the authentic reversibility of the Li anode in a specific LMB, regardless of the origin of the influential factors (key materials, assembling procedures, testing protocols, etc.).

The variations of $R_{Li,n}$, $IRL_{inactive\ Li,n}$ and $IRL_{SEI,n}$ (**Figure 3g-i**) along with cycling demonstrate that the reversibility of LMAs upon cycling are jointly determined by the inherent irreversibility and its related incremental coefficient. $IRL_{inactive\ Li}$ at 400 kPa and 800 kPa only slightly increases when compared to that at 100 kPa, suggesting that high stack pressure mainly avoids the deterioration of electron and ion transportation owing to less dendritic electro-deposition morphology. However, its function for minimizing SEI cracking possibilities is inconspicuous. It is believed that stack pressure can no longer suppress dendritic morphology from the mechanical-electrochemical perspective when thick and porous "dead Li" layer is formed. According to the small increment of inactive Li (0.1 mg, Supplementary Table 8) from the 25th to the 50th cycle under 800 kPa, it also demonstrates that high stack pressure ameliorates aggregation between "dead Li" particles[18] to enable more easier electron transportation[38]. Long-term cycling will also be benefited from re-utilization of inactive Li from dense "dead Li" layer.[29,43] Except for that, according to the mathematical hypothesis, knowing values of $IRL_{Li,0}$ and K_{IRL} theoretically enables failure prediction for practical LMBs. As shown in Supplementary Fig. 11, a 0.9Ah Li/NCM811 pouch cell cycled under C/5 and 100 kPa encounters sudden capacity drop at the 69th cycle. The thickness of the residual active Li is 37 μm (theoretically calculated to be near 3.0 mg of active Li remaining) as determined by SEM. The mathematical modeling based on the quantitative analysis results of this cell predicts that critical failure occurs after ~80 cycles (Supplementary Fig. 12), which is in good agreement with the realistic test results and reflects the practicality of this method in assessing the potential level of LMBs without long-term cycling.

Quantitative measurement for degradation analysis of LMA in practical LMBs

Inactive Li is mostly originated from detached Li dendrites during root-preferred stripping process; thus, quantification of inactive Li will offer deeper understanding of the degradation mechanism of LMA. As shown in **Figure 4a**, both CE_{cell} and the capacity of the cell under C/2 decay much faster than those under C/5 (both of them

have no constant voltage charging process), and the cell completely fails only after 25 cycles (Supplementary Fig. 11a, b). This result is quite unusual, since the corresponding areal current density to the rate of C/5 and C/2 is 0.75 mA/cm^2 and 1.87 mA/cm^2, respectively, both of which are quite mild testing conditions in the case of coin-type cells. The much worse rate capability of pouch cells than that of coin cells strongly suggest that the degradation behavior of LMAs in pouch cells can't be simply learned from that in coin cells. Applying the analytical method proposed in this work, it is revealed that the mass of inactive Li increases dramatically at the rate of C/2, which is the main cause of the rapid failure of the cell (**Figure 4b**). In contrast, the quantity of inactive Li after 50 cycles at the rate of C/5 is less than 40% of that at C/2, and all data points are located below the dash line, demonstrating significantly improved stability of the Li anode when the rate is reduced from C/2 to C/5. Also, the average error of the mass of inactive Li at C/2 (7%) is more than three times higher than that at C/5 (2%), implying the existence of large and unevenly distributed protrusions and pits over the entire anode after cycling at C/2 due to rapidly deteriorated stripping/plating behavior of Li in practical cells when the current density is enlarged.[44] Furthermore, both the values of $IRL_{inactive\ Li,0}$ and $K_{inactive}$ increases enormously when the rate is raised from C/5 to C/2 (**Figure 4c and d,** and Supplementary Fig. 13c). High $IRL_{inactive\ Li,0}$ (2.01%) at the rate of C/2 demonstrates serious irreversibility of Li plating and stripping at each cycle,[45,46] while high $K_{inactive}$ (~0.06) indicates the incremental part for irreversibility grows quickly due to accumulation of large quantities of "dead Li" particles, which in turn aggravates dendritic Li growth. As plotted in **Figure 4e**, the total thickness of the "dead Li" layer on both sides of the Li anode quickly exceeds 300 μm only after 25 cycles at C/2, which is almost twice than that at C/5. Even after 50 cycles, the thickness of the "dead Li" layer only reaches 230 μm at C/5. The average thickness increment for the "dead Li" layer under C/2 (~12.4 μm/cycle) is nearly three times larger than that of C/5 (4.6 μm/cycle) (**Figure 4f**). In addition, the mass of active Li measured by the quantitative analysis method is quite coincident with its thickness observed from the SEM images (Supplementary Fig. 14-21), confirming the accuracy of this

quantification method, and suggesting fast consumption of active Li under C/2. Furthermore, FIB-SEM image of the Li anode after 25 cycles at C/5 (**Figure 4g**) displays compact accumulation state of "dead Li", whereas that at C/2 (**Figure 4h**) shows loosely packed "dead Li" with obviously higher porosity, which explains the much more serious thickness expanding of the Li anode at higher rates.

Combining the quantitative analysis data and the conventional qualitative morphology characterization results, deeper understanding of the compositional and structural evolution of LMAs under different charge/discharge rates can be established as illustrated in **Figure 4i** and **j**. At a low rate of C/5, low $IRL_{inactive\ Li,0}$ of 0.40% enables relatively flat Li deposition with few mossy morphologies. The quantified results display little fluctuation on the mass of inactive and active Li, which means less "dead Li" and uniform stripping from the pristine LMA.[47-49] Thereby, parasitic effects from "dead Li" will be slowly initiated and accumulated as reflected by the low incremental coefficient ($K_{inactive}$) of 0.017. After 10 cycles, little increment of $IRL_{inactive\ Li,n}$ to 0.47% (n=10), which represents compact agglomeration of "dead Li", predicts that continuous stripping/plating of Li will be hardly disturbed by concentration polarization from highly porous and thick electrode structures. In significant contrast, increasing the rate to C/2 induces serious inhomogeneity of charge distribution resulting in porous interphase growth over the anode, which is responsible for the high inherent $IRL_{inactive\ Li,0}$ of 2.01% and thus massive and fast growth of dendritic Li.[34,47] A large amount of inactive Li particles are quickly formed by the detachment of dendritic Li protrusions, while compensation of Li for the cathode creates large and random pits in LMA, giving rise to large measurement error (~7.0%) of inactive Li mass.[32] Highly porous and thick "dead Li" layers result in serious mass transportation issues which induce problematic exhaustion of Li-ions and hindrance of electron transport. Thereafter, severe cumulative parasitic effects as reflected by a high incremental coefficient ($K_{inactive}$) of 0.06 cause extremely unstable plating behavior to form larger Li dendrites, giving rise to a high $IRL_{inactive\ Li,15}$ of 4.96% only after 15 cycles. Meanwhile, heavily charged locations will dynamically move to more curved surface to initiate new electron concentrated areas

that intensify the inhomogeneity of Li plating/stripping [50]. Finally, fast exhaustion of active Li results in total failure of the cell. These findings suggest that the current density on the LMA needs extensive optimization for long cycle life, which is essential to enable a high-loading cathode in LMB for high energy density LMB, or to achieve fast charge LMB cell for practical applications.

Conclusions

In summary, a novel and universal analytical method is proposed to quantitatively distinguish active Li from inactive ones in cycled LMA, which enables to decouple the proportions of authentic reversibility and irreversibility of Li anode for practical LMBs. By establishing a quantitative test method of active and inactive Li separately and the corresponding mathematical hypothesis, a set of key parameters is created to quantitatively describe the hidden behavior of Li plating/stripping in practical cells. The application of this new method on practical Ah-level pouch cells can reveal the differences in the true reversibility of the Li anode under different conditions, including stack pressure and charge/discharge rate. Moreover, combining with morphological characterization, the structural evolution and degradation process of LMA in practical LMBs can be revealed in a more quantitative way. We believe that this method will become a powerful tool to deeply understand the electrochemical behavior of LMA, and set a new and universal criterion to assess the authentic reversibility of LMBs, which is extremely essential to the development of high performance LMBs towards practical applications.

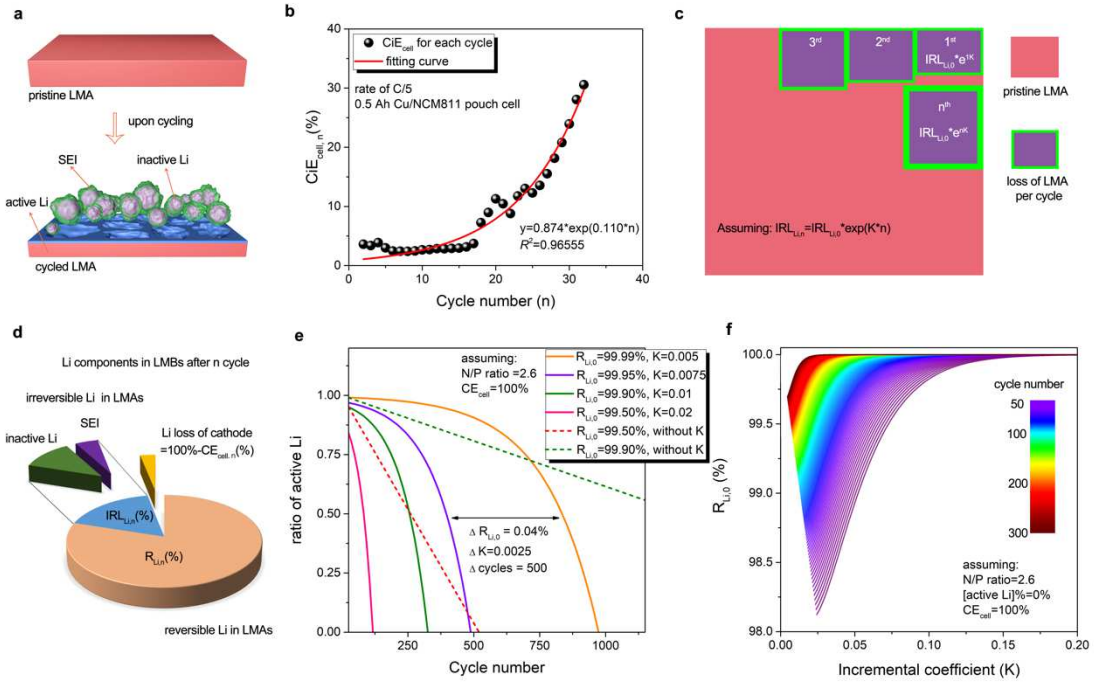

Figure 1. (a) Illustration of the composition and morphology of pristine LMA and LMA after cycling. The porous "dead Li" layer above the remaining active Li is composed of SEI-encapsulated inactive Li. The inactive Li doesn't include the irreversible Li compounds in the SEI. (b) The Coulombic inefficiency (CiE_{cell}) *vs.* cycle number (n) of a 0.5 Ah Cu/NCM811 pouch cell and the corresponding fitting curve based on an exponential function. The high value of R^2 (0.9655) indicates good reliability of the fitting function. (c) The diagram showing the continuously increasing consumption of active Li per each cycle in practical LMBs by considering the parameter of K_{IRL} (abbreviated as K in the diagram). The value of $IRL_{Li,n}$ rises along with the increase of the cycle number (n), as it contains the cumulative parasitic effects from the "dead Li" layer formed within the (n-1) cycles. (d) A pie chart displaying the Li components in cycled LMBs after the n^{th} cycle. The average CE of the cell reflects the reversibility of the cathode. (e) The differences in lifetime prediction of LMBs by applying $R_{Li,0}$ in perfect and calibrated conditions with different incremental coefficients (K). The N/P ratio of 2.6 is applied as it is the real value for Li/NCM811 pouch cells used in this work. (f) The requirements for $R_{Li,0}$ and the incremental coefficient (K) to achieve the lifetime target under specific conditions. This cycle number map established under a certain condition can also be used for lifetime prediction of practical LMBs by applying

specific $R_{Li,0}$ and K.

Table 1. The index system composed of several quantitative parameters as a criterion to assess the reversibility and irreversibility of the Li anode in LMBs.

Abbreviation	Representation
$IRL_{Li,0}$	proportion of the inherent irreversible Li loss in LMA
$IRL_{Li,n}$	proportion of the irreversible Li loss in LMA after n cycles
$IRL_{inactive\ Li,0}$	proportion of the inherent irreversible Li loss due to the formation of the inactive Li
$IRL_{SEI,0}$	proportion of the inherent irreversible Li loss due to the formation of SEI formation
$R_{Li,0}$	proportion of the inherent reversible Li in LMA
K_{IRL}	the incremental coefficient that describes the impact of the irreversible Li on $IRL_{Li,n}$

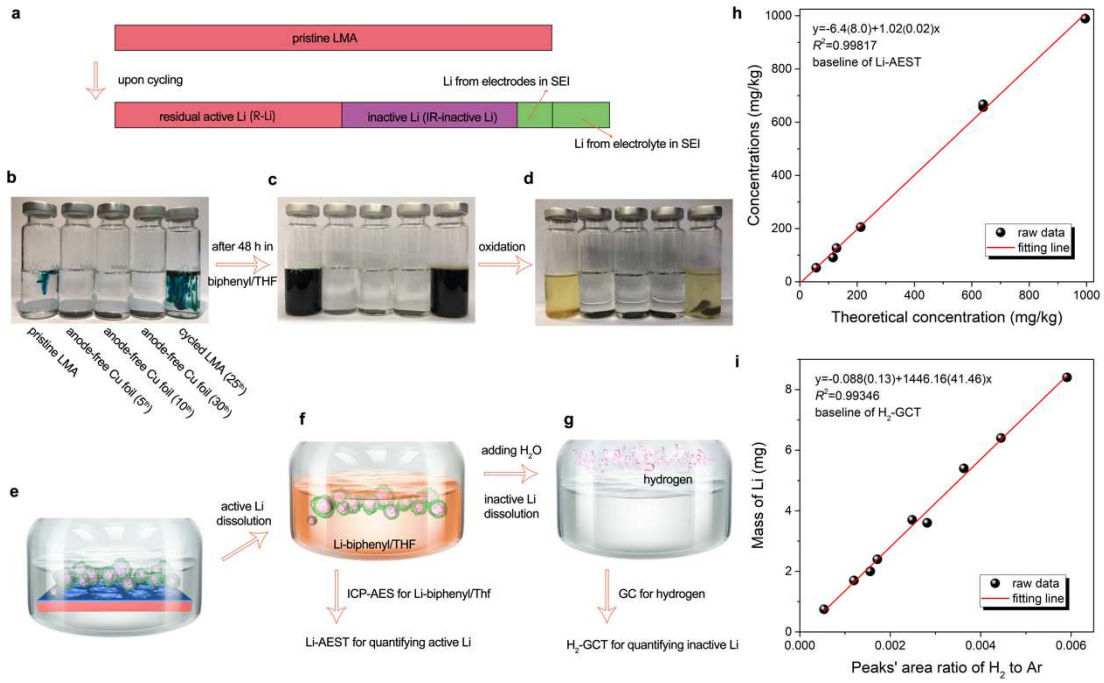

Figure 2. (a) The components of LMA before and after cycling. The amounts of active Li and inactive Li are the key data to quantify the parameters of $R_{Li,0}$, $IRL_{Li,0}$ and K_{IRL} according to our mathematical hypothesis. (b-d) Digital photographs displaying the stability of different types of active and inactive Li in the biphenyl/THF solution, including pristine LMA, Cu foils from anode-free Cu/NCM811 pouch cells and cycled LMA from Li/NCM811 pouch cells. 0.5Ah Cu/NCM811 pouch cells were assembled and cycled under 200 kPa-C/5 for 5/10/30 cycles to acquire the "dead Li" layer. The electrochemical performances for each cell are shown in Supplementary Fig. 5. Cycled LMA are obtained from a 0.5 Ah Li/NCM811 pouch cell charge/discharged under 100 kPa-C/2 for 10 cycles. The color change from transparent to dark blue observed in the leftmost and rightmost bottles is caused by the dissolution of exposed metallic Li in biphenyl/THF. No color change of the other three bottles indicates that SEI encapsulated inactive Li is insoluble in biphenyl/THF. After full dissolution and oxidation, no residual solids are observed in the leftmost bottle which contains pure Li in the beginning, while solid residues still exist in other four bottles, which are insoluble SEI encapsulated inactive Li. (e-g) The diagram showing the procedures for decoupling and quantitative analysis of active and inactive Li in cycled LMA. Circular cycled LMAs (diameter of 14 mm) along with separators were punched and rinsed to remove

residual Li salt (Supplementary Table 1) to collect metallic Li plated on the separator and to eliminate the interference of residual electrolyte. (e) Cycled LMAs were submerged in the biphenyl/THF solution and sealed by rubber plugs in air-tight bottles (Supplementary Fig. 4) which were then placed at room temperature for at least 24 h before further characterization to guarantee the full dissolution of the active Li. (f) After full dissolution of the active Li, certain mass of Li-biphenyl/THF solution was taken out from the air-tight bottle and subjected to thermal digestion for the quantitative measurement of the mass of the active Li through Li-AEST. (g) A certain amount of deionized water was injected to the air-tight bottle across the rubber plug to react with the inactive Li. The generated hydrogen was quickly sampled by using an air-tight syringe and injected to gas chromatography (GC) for quantifying the mass of the inactive Li. Detailed descriptions about the step-by-step procedures and related calculations can be found in **Methods**. (h) The baseline of Li-AEST and (i) that of H_2-GCT obtained by fitting the quantitative analysis data points of standard solutions of Li dissolved in biphenyl/THF and Li dissolved in water, respectively. The fitting results are shown in the inset of two figures.

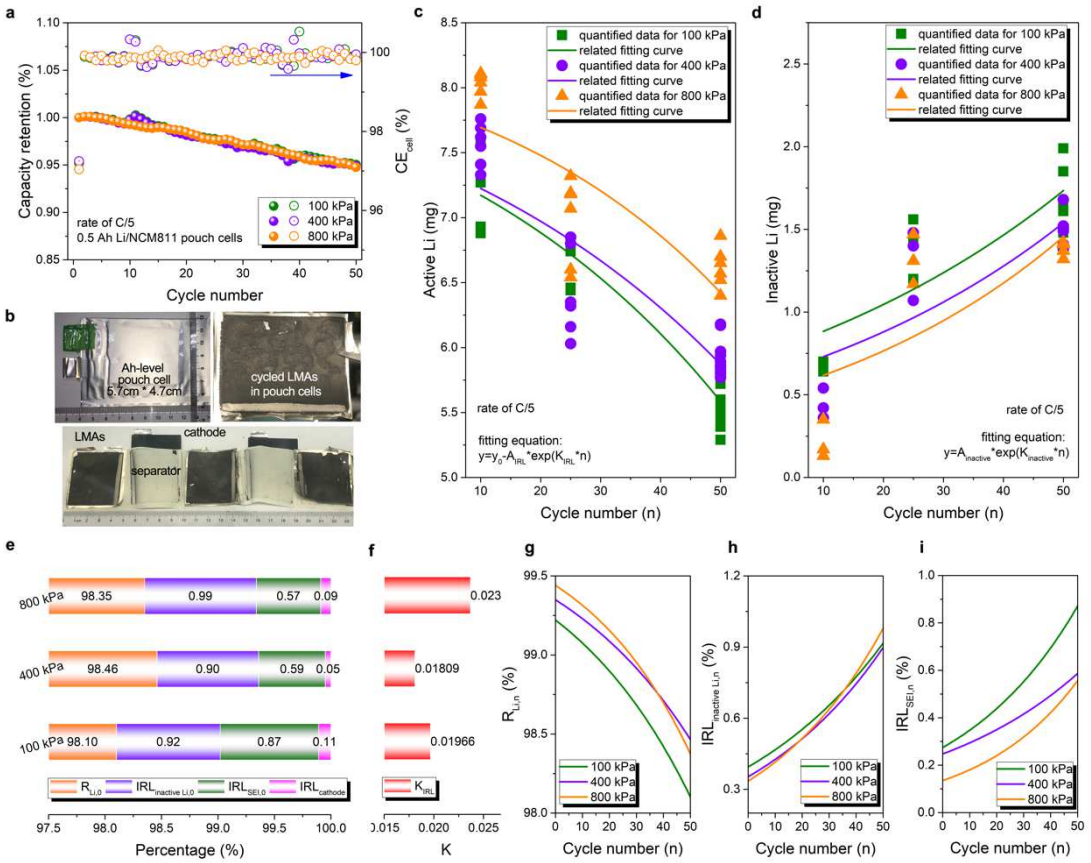

Figure 3. (a) The plots of capacity retention *vs.* cycle number and CE_{cell} *vs.* cycle number of practical 0.5 Ah Li/NCM811 pouch cells operated under different stack pressures at the rate of C/5. The data of the first cycle run at C/20 for the activation of the cells isn't included. (b) Photographs of a 0.5 Ah Li/NCM811 pouch cell and the corresponding LMAs disassembled from the cycled cell. (c) The quantitatively measured masses of the active Li in the LMAs from the 0.5 Ah Li/NCM811 pouch cells cycled for 10, 25 and 50 times under different stack pressures, and the corresponding fitting curves of active Li mass *vs.* cycle number (n) based on the exponential function. (d) The quantitative analysis of the masses of the inactive Li in the same LMAs as those in (c) and the corresponding fitting curves. All the raw data of Li-AEST and H_2-GCT measurements are listed in Supplementary Table 7-10. The fitting was conducted based on 6 sets of data points measured independently at the same conditions to acquire the statistical average results. (e) The values of $R_{Li,0}$, $IRL_{inactive\ Li,0}$, $IRL_{SEI,0}$ and $IRL_{cathode}$ (irreversible Li loss in the cathode), and (f) the values of K_{IRL} for the 0.5 Ah Li/NCM811 pouch cells under different stack pressures. The mathematically modeled

curves of (g) $R_{Li,n}$ vs. cycle number (n), (h) $IRL_{inactive\ Li,n}$ vs. cycle number (n) and (i) $IRL_{SEI,n}$ vs. cycle number (n) for the pouch cells under different stack pressures.

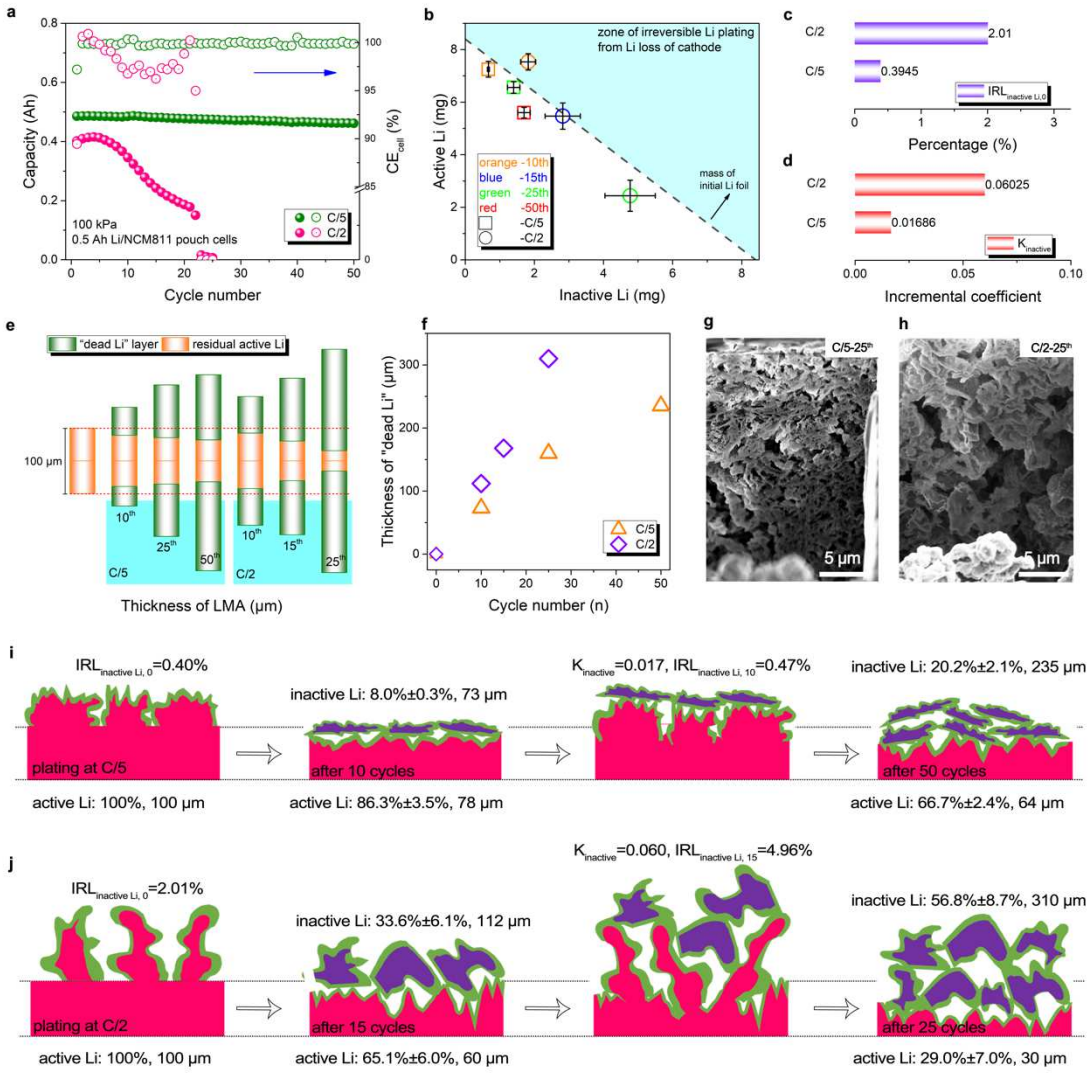

Figure 4. (a) The plots of capacity vs. cycle number (n) and CE_{cell} vs. cycle number (n) of 0.5 Ah Li/NCM811 pouch cells cycled at C/2 and C/5 with the stack pressure of 100 kPa. The data of the first cycle run at C/20 for the activation of the cells isn't included. (b) Quantified results of the masses of the active and the inactive Li in the LMAs from the 0.5 Ah Li/NCM811 pouch cells disassembled after 10, 25 and 50 cycles at C/2 and C/5. The data point (C/2-10 cycles-100kPa) above the dash line (corresponding to the initial Li foil mass of ~8.4 mg, Supplementary Table 6) shows that the total mass of the active and inactive Li exceeds the original mass of the Li foil, suggesting that the additional Li due to the irreversible capacity loss of the cathode was plated inside the porous anode[51,52], which is also confirmed by the relatively lower CE_{cell}. After 25 cycles at C/2, the masses of the active and inactive Li at 100 kPa are 2.44±0.59 mg and

4.69±0.60 mg, respectively. Owing to the high accuracy of this method, error values for quantified data may qualitatively indicate the homogeneity of Li components across LMAs. (c) The values of $IRL_{inactive\ Li,0}$ and (d) the values of the correlated incremental coefficient ($K_{inactive}$) derived from the quantified data of the inactive Li. (e) The thicknesses of the "dead Li" layers (on both sides) and the remaining active Li in LMAs cycled for different times at C/5 and C/2, which are measured by SEM. (f) The increments of "dead Li" layer thickness along with the cycle number. (g) The FIB-SEM image showing the morphology of the "dead Li" layer on the surface of the LMA cycled for 25 times at C/5, and (h) that at C/2. (i), (j) The diagrams demonstrating the morphology evolution and the degradation processes of LMAs in practical LMBs during cycling at the rates of C/5 (i) and C/2 (j), which are drawn based on both the quantitative analysis data and the qualitative morphological characterizations. The red and the purple regions correspond to the active and the inactive Li, respectively, while the green ones correspond to the SEI.

Methods

Materials. Tetrahydrofuran (THF, anhydrous, purity≥99.9%, inhibitor-free) and biphenyl (purity≥99.0%) were purchased from Sigma-Aldrich. Before using, all the THF solvent was handled by molecular sieve to remove the residual water. The electrolyte was composed of 1.0 M $LiPF_6$ in FEC/EMC (in *vol.* ratio 1:5). 45 μm and 100 μm Li foil were employed as the anodes. NCM811 cathodes and LR-NCM cathodes were kindly provided by Ningbo FuLi Battery Material Technology Co., Ltd.

Pouch cell assembly and electrochemical tests. To achieve the requirements for practical LMBs, both 45 μm Li foils (placed only on the top and at the bottom) and 100 μm Li foils (used as the inner anodes) were employed as the anodes (4.7 cm × 5.7 cm, excluding the area of the tap) to reach the required N/P ratios. 3 pieces of either double-coated NCM811 (areal loading of 20.0 mg cm^{-2} on one side) or double-coated LR-NCM (areal loading of 21.5 mg cm^{-2} on one side) with tailor-made dimensions (4.3 cm × 5.3 cm) were employed as the cathodes. The cells were encapsulated in aluminum packing foil (areal loading of 3.27 mg cm^{-2}) by hot-pressing, followed by electrolyte injection with the dosage of 4.0 g Ah^{-1}, and connection of the taps (Ni and Al strips) using a laser welding machine. Before electrochemical tests, certain stack pressures were applied on these pouch cells (Supplementary Fig. 3a, b) by using a home-made pressurizing equipment and cell-holders (Supplementary Fig. 3c, d). Pouch cells with certain stack pressures in cell-holders were connected to LANHE-CT2001A system (Jinnuo Wuhan Corp., Wuhan, China). For the Li/NCM811 pouch cells, the charge/discharge rates were set at C/5 and C/2 (1 C equals to 600 mA) between the voltage of 2.6 V and 4.3 V. For the Li/LR-NCM pouch cells, the charge/discharge rate was set at C/5 (1 C equals to 750 mA) between the voltage of 2.6 V and 4.6 V. Detailed parameters for the assembly of practical pouch cells could also be seen in our previous work[13].

Characterizations. The inductively coupled plasma-atomic emission spectrometry (ICP-AES, Optima 2100) was employed in the Li-AEST method. The gas

chromatography (Agilent Technologies 7890B) was used to quantifying the amount of hydrogen. SEM (Hitachi S-4800 field emission scanning electron microscope) and focused ion beam SEM (FIB-SEM, Auriga produced by Carl Zeiss) was used to characterize the morphology of LMAs after cycling.

Analytical methodology. Detailed procedures for quantitative analysis of the active and inactive Li in cycled LMAs are described as follows.

1) Three disks (14 mm in diameter) obtained by punching three different areas in each cycled LMA taken out from the pouch cells were rinsed for three times with THF (10 mL) to remove the residual $LiPF_6$ which may interfere the Li-AEST results (Supplementary Fig. 4a), and then dried in an Ar-filled glove box before quantitative measurement. Anode-free coin cells (Li/Cu cells) were also tested to characterize the stability of SEI against biphenyl/THF, however, our results demonstrated the residues on Cu foil obtained from Li/Cu cells didn't seem to be pure inactive Li. Consequently, all analytical procedures were performed on cycled LMAs from Ah-level pouch cells. Not enough data have been obtained to verify whether this method can also be effectively applied for coin cells.

2) 10 mL of biphenyl/THF (with 6.0 *wt.*% of biphenyl) was added into the air-tight glass bottle containing a disk sample obtained in the first step to dissolve the active Li. The cycled LMAs were punched to form smaller pieces (14 mm in diameter) for quantitative analysis, hence the fresh punching boundaries of active Li (Li bulks) was exposed without SEI coverage. It is the place that the biphenyl/THF solution contacts with residual bulk Li (active Li). At the same time, the inactive Li ("dead Li") particles locating at the punching boundaries were also broken and would be dissolved by biphenyl/THF. However, the proportion of the broken inactive Li particles is relatively small. Assuming the average diameter of "dead Li" particles is 20 μm (0.02 mm), the total mass of the broken inactive Li particles at the boundary of the punched samples is estimated to 0.011 mg, while the mass of Li foil with diameter of 14 mm is 8.4 mg. Therefore, the mass of dissolved inactive Li can be neglected. After a certain period at

25 ℃, the mass of the whole Li-biphenyl/THF solution was recorded as m_{target} (gram as the unit). A given volume of Li-biphenyl/THF solution (2 mL) was then quickly sampled. To ensure the accuracy of the results measured by ICP-AES, the sampled liquid was quickly injected to pure THF (m_{dilute}, gram as the unit) and sealed. The whole mass of Li-biphenyl/THF after diluting was precisely weighed using a microbalance and recorded as $m_{solution}$ (gram as the unit). Each sampled solution was then used for two parallel digestions; the mass of the digestion liquid was precisely weighed using a microbalance and recorded as $m_{digestion}$ (gram as the unit). After full evaporation of THF from samples for digestions, the digestion was carried out by heating the solution occurred under hydrothermal with HNO_3 (4.5 mL), H_2O_2 (0.75 mL) and $HClO_4$ (0.75 mL) at 180 ℃ for 4 h in an autoclave after pre-heating for 30 min at 80 ℃ under air atmosphere. The aqueous solution after digestion was carefully collected and diluted with deionized water in a volumetric flask (V_{flask} of 25.0 mL, which was then subjected to ICP-AES measurement ($C_{ICP-AES}$, milligram/liter as the unit) to quantify the concentration of Li in the original Li-biphenyl/THF solution. The equation for calculating the mass of active Li ($m_{active\ Li}$, milligram as the unit) is expressed in Equation 6.

$$m_{active\ Li} = \frac{C_{ICP-AES} * m_{solution} * m_{target} * V_{flask}}{1000 * (m_{solution} - m_{dilute}) * m_{digestion}} \quad 6$$

3) A given amount (2.0 mL) of deionized water was injected into the same air-tight bottle used in step 2 by a 5.0 mL air-tight syringe (Supplementary Fig. 4b). The generated gas was quickly sampled using a 25 mL air-tight syringe (Supplementary Fig. 4c), followed by the injection into a vacuum and air-tight Al foil packing bag (Supplementary Fig. 4d). The gas in the bag was then injected to the GC equipment for quantifying the mass of the inactive Li in "dead Li". Hydrogen is the only gas generated by the reaction of pure Li with water (Supplementary Fig. 8a). But as shown in Supplementary Fig. 8d, the SEI formed in cycled LMAs will also react with water to release CO_2, CH_4, C_2H_4 and C_2H_6. The generation of additional gases besides hydrogen will affect the molar ratio of H_2 in the sample gases, interfering the peak area related to hydrogen for further quantitative measurement of hydrogen. Therefore, the calibration

curve (such as the curve in Supplementary Fig. 9a) established using pure Li foil with known weight is not able to accurately measure the inactive Li from cycled LMAs. Fortunately, we found that argon which has a fixed content amount in all samples, could be used as a reference gas for internal calibration. After sealing in the Ar-filled glove box, the volume of Ar in the gas sample is kept unchanged during the entire measuring process. The integral area of the peaks related to H_2 ($S_{hydrogen-test}$) and that of Ar ($S_{argon-test}$) in GC-MS spectra were automatically calculated by the software, respectively. Therefore, we could use the molar ratio of H_2/Ar instead of the ratio of H_2/all gases for quantitative analysis. Namely, during the whole H_2-GCT process, the mole of H_2 ($n_{hydrogen}$), the mole of Ar (n_{argon}), the integral area of H_2 ($S_{hydrogen}$) and the integral area of Ar (S_{argon}) follow Equation 7,

$$\frac{n_{hydrogen}}{n_{argon}} = \frac{S_{hydrogen}}{S_{argon}} \cdot C \quad (7)$$

where C represents the constant between molar ratio and integral area in H_2-GCT. Five calibrating gases including different ratios of hydrogen, nitrogen and argon are used (detailed ratios are listed in Supplementary Table 5) to calculate C. The GC-MS spectra of different calibrating gases are shown in Supplementary Fig. 9d.

Despite that constant C can be acquired by applying different calibrating gases, actually, the exact mole of Ar is not clear in the bottle. Thus, pure Li foils with known masses and pure THF with the same volume as that of the residual liquid are employed as the reference to characterize the mole of Ar here.

For pure Li, the equation is listed below.

$$\frac{n_{hydrogen}}{n_{argon}} = \frac{n_{pure\ Li}}{n_{argon-pure\ Li}} = \frac{S_{hydrogen-pure\ Li}}{S_{argon-pure\ Li}} \cdot C \quad (8)$$

For cycled LMA sample, the equation is listed below.

$$\frac{n_{hydrogen}}{n_{argon}} = \frac{n_{active\ Li}}{n_{argon-test}} = \frac{S_{hydrogen-test}}{S_{argon-test}} \cdot C \quad (9)$$

As the volume of Ar keeps unchanged between the reference samples and the tested samples, the molar ratio of H_2 to Ar in two cases is proportional to the mass ratio of pure Li foil to the inactive Li in cycled LMAs. Thus, the calibrated and modified calculation equation for precise measuring the mass of inactive Li is expressed in

Equation 10, where $S_{argon-pure\ Li}$, $S_{hydrogen-pure\ Li}$ and $m_{pure\ Li}$ are the parameters with known average values according to the calibration experiments.

$$m_{active\ Li} = \frac{S_{hydrogen-test}}{S_{argon-test}} \cdot \frac{S_{argon-pure\ Li}}{S_{hydrogen-pure\ Li}} \cdot m_{pure\ Li} \quad 10$$

Mathematical hypothesis and related equations. In practical LMBs, CE_{cell} is apparently representative for the cathode instead of $R_{Li,n}$ due to the compensation of the irreversible Li loss in the anode from the Li sources in LMAs. Before active Li was exhausted, the Coulombic efficiency measured by electrochemical charge/discharge curves is related to the irreversible Li loss in the cathode ($IRL_{cathode,n}$). Therefore, $IRL_{cathode,n}$ can be directly acquired from the Coulombic efficiency ($CE_{cell,n}$) of the Li metal pouch cell as follows,

$$IRL_{cathode,n} = 100\% - CE_{cell,n} \quad 11$$

The total Li amount utilized in one charge/discharge cycle in a full cell is composed of reversible Li (active Li), Li species in SEI, inactive Li encapsulated by SEI and irreversible Li loss in the cathode. Hence

$$R_{Li,n} + IRL_{SEI,n} + IRL_{inactive\ Li,n} + IRL_{cathode,n} = 100\% \quad 12$$

The mathematical relationship between reversible and irreversible parts in LMBs are discussed below. As $IRL_{Li,n}$ is composed of $IRL_{SEI,n}$ and $IRL_{inactive\ Li,n}$, the CE_{cell} at the n^{th} cycle can be expressed as Equation 13 and 14.

$$CE_{cell,n} = R_{Li,n} + IRL_{SEI,n} + IRL_{inactive\ Li,n} \quad 13$$

$$IRL_{Li,n} = IRL_{SEI,n} + IRL_{inactive\ Li,n} \quad 14$$

To clearly demonstrate the mathematical relationship between the cycle number and the content of active Li, several parameters are defined as follows. The capacity ratio of the negative electrode to the positive electrode (N/P ratio) is named as [N/P]. y_0 (mg) is defined as the initial mass of pure Li foil (8.4 mg for the mathematical fitting as indicated in Supplementary Table 6), and y_n (mg) the mass of active Li in cycled LMAs after n cycles. The corresponding total Li mass in the cathode is $\frac{y_0}{[\frac{N}{P}]}$ mg. Theoretically, consumption of Li in each cycle is related to $IRL_{Li,n}$. So the relationship between the mass of residual active Li and cycle number should be coincident with

Equation 15. In ideal conditions, as $IRL_{Li,n}$ equals to $IRL_{Li,0}$, Equation 15 can be expressed as Equation 2.

$$y_n = y_0 - \left(\frac{y_0}{\lceil \frac{N}{P} \rceil}\right) * IRL_{Li,n} * n \quad (15)$$

$$[active\ Li]\% = 1 - \left(\frac{1}{\lceil \frac{N}{P} \rceil}\right) * IRL_{Li,0} * n \quad (2)$$

But this ideal linear relationship is affected by the cumulative effects from additional "dead Li" layer, causing the deviation of $IRL_{Li,n}$ from the initial one ($IRL_{Li,0}$). As a result, Equation 2 and 15 are not suitable to describe the relationship accurately. In described in the main text, the irreversibility can be expressed by two parts as Equation 1, namely the inherent part and the incremental part. Herein, to describe the incremental degree induced by the cumulative effects, the incremental coefficient (K) is introduced in the form of exponential function to calibrate the above linear relationship. Due to the addition relationship instead of multiplying one regarding the consumption principle of active Li in practical LMBs, the modified mathematical equation after n cycles is expressed below.

$$IRL_{Li,n} = IRL_{Li,0} * e^{K_{IRL}*n} \quad (1)$$

$$y_n = y_0 - \left(\frac{y_0}{\lceil \frac{N}{P} \rceil}\right) * IRL_{Li,0} * [e^{K_{IRL}*1} + e^{K_{IRL}*2} + \cdots + e^{K_{IRL}*n}] \quad (16)$$

Equation 16 can be further expressed in the form of integration as Equation 17. Equation 17 can also be expressed as the relationship between the retention ratio of active Li ([active Li]%) and the cycle number as Equation 3.

$$y_n = y_0 - \left(\frac{y_0}{\lceil \frac{N}{P} \rceil}\right) * \left(IRL_{Li,0}\right) * \frac{1}{K_{IRL}} * e^{K_{IRL}*n} \quad (17)$$

$$[active\ Li]\% = 1 - \left(\frac{1}{\lceil \frac{N}{P} \rceil}\right) * IRL_{Li,0} * \frac{e^{K_{IRL}*n}}{K_{IRL}} \quad (3)$$

Equation 17 can be further simplified as

$$y_n = y_0 - A_{IRL} * e^{K_{IRL}*n} \quad (18)$$

where

$$A_{IRL} = \left(\frac{y_0}{\left[\frac{N}{P}\right]}\right) * IRL_{Li,0} * \frac{1}{K_{IRL}} \quad 19$$

By knowing the values of A_{IRL} and K_{IRL} from the fitting results, the values of $IRL_{Li,0}$ can be obtained.

To describe the variation of the inactive Li during cycling, the same mathematical model as that used for describing the active Li can be applied. The mass of inactive Li after n cycles (Z_n) is expressed in Equation 20 and 21, and the expression of the percentage of inactive Li is listed in Equation 4. $K_{inactive}$ is the incremental coefficient for $IRL_{inactive\ Li,0}$.

$$Z_n = \left(\frac{y_0}{\left[\frac{N}{P}\right]}\right) * \left(IRL_{inactive\ Li,0}\right) * \frac{1}{K_{inactive}} * e^{K_{inactive}*n} \quad 20$$

$$Z_n = A_{inactive} * e^{K_{inactive}*n} \quad 21$$

$$[inactive\ Li]\% = \left(\frac{1}{\left[\frac{N}{P}\right]}\right) * IRL_{inactive\ Li,0} * \frac{e^{K_{inactive}*n}}{K_{inactive}} \quad 4$$

Data availability

The datasets analyzed and generated during the current study are included in the paper and its Supplementary Information.

Acknowledgements

This work was supported by National Natural Science Foundation of China (Grant No. 52001320, 51872305), "Lingyan" Research and Development Plan of Zhejiang Province (Grant No. 2022C01071), and China Postdoctoral Science Foundation funded Project (Grant No. 2019TQ0331, 2019M662123). Dr. Ying Shirley Meng acknowledges funding support from the Zable Endowed Chair of Energy Technology and the Sustainable Power & Energy Center of UC San Diego. Dr. Wei Deng thanks for the helpful discussions from Mr. Fei Zhao about analytical procedures and Mr. Qiang Guo about mathematical equations, and thanks Mr. Zixin Jiang, Mr. Qigao Han and Mr.

Wei Fang for the helps on pouch cell assembly. Dr. Wei Deng thanks the kind helps from Mrs. Yingying Han for GC analysis, Mr. Yafei Li for Ar-BET characterizations, and Ms. Kai Shen for ICP-AES analysis from the testing center of NIMTE, CAS.

Author contributions

W.D., X.Z., Y. S. Meng and Z.L. conceived the concept and the project. W.D. performed all the analytical procedures and data analysis. W.D. and X.Y. performed the ICP-AES characterizations. W.D., H.Z, B.H. assembled and tested the pouch cells. W.D., W.B., X.Z., B.Q., Y. S. Meng and Z.L. wrote and revised the manuscript. All authors discussed the results and reviewed the manuscript.

Additional information

Supplementary information The online version contains supplementary material available at_____.

Reference

1 Liu, J. *et al.* Pathways for practical high-energy long-cycling lithium metal batteries. *Nature Energy* **4**, 180-186, doi:10.1038/s41560-019-0338-x (2019).

2 Albertus, P., Babinec, S., Litzelman, S. & Newman, A. Status and challenges in enabling the lithium metal electrode for high-energy and low-cost rechargeable batteries. *Nature Energy* **3**, 16-21, doi:10.1038/s41560-017-0047-2 (2017).

3 Chen, S. *et al.* Critical Parameters for Evaluating Coin Cells and Pouch Cells of Rechargeable Li-Metal Batteries. *Joule* **3**, 1094-1105, doi:10.1016/j.joule.2019.02.004 (2019).

4 Chen, S., Dai, F. & Cai, M. Opportunities and Challenges of High-Energy Lithium Metal Batteries for Electric Vehicle Applications. *ACS Energy Letters* **5**, 3140-3151 (2020).

5 Fang, C., Wang, X. & Meng, Y. S. Key issues hindering a practical lithium-metal anode. *Trends in Chemistry* **1**, 152-158 (2019).

6 Zhang, X., Yang, Y. & Zhou, Z. Towards practical lithium-metal anodes. *Chemical Society Reviews* **49**, 3040-3071 (2020).

7 Weber, R. *et al.* Long cycle life and dendrite-free lithium morphology in anode-free lithium pouch cells enabled by a dual-salt liquid electrolyte. *Nature Energy* **4**, 683-689 (2019).

8 Huang, C.-J. *et al.* Decoupling the origins of irreversible coulombic

efficiency in anode-free lithium metal batteries. *Nat. Commun.* **12**, 1-10 (2021).

9 Adams, B. D., Zheng, J., Ren, X., Xu, W. & Zhang, J. G. Accurate determination of Coulombic efficiency for lithium metal anodes and lithium metal batteries. *Advanced Energy Materials* **8**, 1702097 (2018).

10 Xiao, J. *et al.* Understanding and applying coulombic efficiency in lithium metal batteries. *Nature Energy* **5**, 561-568 (2020).

11 Holtstiege, F., Wilken, A., Winter, M. & Placke, T. Running out of lithium? A route to differentiate between capacity losses and active lithium losses in lithium-ion batteries. *Phys. Chem. Chem. Phys.* **19**, 25905-25918 (2017).

12 Niu, C. J. *et al.* Balancing interfacial reactions to achieve long cycle life in high-energy lithium metal batteries. *Nature Energy* **6**, 723-732, doi:10.1038/s41560-021-00852-3 (2021).

13 Deng, W. *et al.* Competitive Solvation-Induced Concurrent Protection on the Anode and Cathode toward a 400 Wh kg–1 Lithium Metal Battery. *ACS Energy Letters*, 115-123, doi:10.1021/acsenergylett.0c02351 (2020).

14 Deng, W., Zhou, X., Fang, Q. & Liu, Z. Microscale lithium metal stored inside cellular graphene scaffold toward advanced metallic lithium anodes. *Advanced Energy Materials* **8**, 1703152 (2018).

15 Kim, M. S. *et al.* Langmuir–Blodgett artificial solid-electrolyte interphases for practical lithium metal batteries. *Nature Energy* **3**, 889-898 (2018).

16 Paul, P. P. *et al.* A Review of Existing and Emerging Methods for Lithium Detection and Characterization in Li-Ion and Li-Metal Batteries. *Advanced Energy Materials*, 2100372 (2021).

17 Fang, C. *et al.* Quantifying inactive lithium in lithium metal batteries. *Nature* **572**, 511-515 (2019).

18 Chen, K.-H. *et al.* Dead lithium: mass transport effects on voltage, capacity, and failure of lithium metal anodes. *J Mater Chem A* **5**, 11671-11681 (2017).

19 Lu, D. *et al.* Failure mechanism for fast-charged lithium metal batteries with liquid electrolytes. *Advanced Energy Materials* **5**, 1400993 (2015).

20 Chandrashekar, S. *et al.* 7Li MRI of Li batteries reveals location of microstructural lithium. *Nat Mater* **11**, 311-315, doi:10.1038/nmat3246 (2012).

21 Gunnarsdóttir, A. B., Amanchukwu, C. V., Menkin, S. & Grey, C. P. Noninvasive In Situ NMR Study of "Dead Lithium" Formation and Lithium Corrosion in Full-Cell Lithium Metal Batteries. *Journal of the American Chemical Society* **142**, 20814-20827 (2020).

22 Aryanfar, A., Brooks, D. J., Colussi, A. J. & Hoffmann, M. R. Quantifying the dependence of dead lithium losses on the cycling period in lithium metal batteries. *Phys. Chem. Chem. Phys.* **16**, 24965-24970 (2014).

23 McShane, E. J. *et al.* Quantification of Inactive Lithium and Solid–Electrolyte Interphase Species on Graphite Electrodes after Fast Charging.

ACS Energy Letters **5**, 2045-2051 (2020).

24 Janakiraman, U., Garrick, T. R. & Fortier, M. E. Lithium Plating Detection Methods in Li-Ion Batteries. *Journal of the Electrochemical Society* **167**, 160552 (2020).

25 Hsieh, Y.-C. *et al.* Quantification of Dead Lithium via In Situ Nuclear Magnetic Resonance Spectroscopy. *Cell Reports Physical Science* **1**, 100139 (2020).

26 Xiang, Y. *et al.* Operando Tracing and Quantifying Inactive Li in Lithium Metal Battery. (2020).

27 Gunnarsdóttir, A. B., Vema, S., Menkin, S., Marbella, L. E. & Grey, C. P. Investigating the effect of a fluoroethylene carbonate additive on lithium deposition and the solid electrolyte interphase in lithium metal batteries using in situ NMR spectroscopy. *J Mater Chem A* **8**, 14975-14992 (2020).

28 Fang, C. *et al.* Pressure-tailored lithium deposition and dissolution in lithium metal batteries. *Nature Energy* **6**, 987-994 (2021).

29 Zheng, J. *et al.* Physical orphaning versus chemical instability: is dendritic electrodeposition of Li fatal? *ACS Energy Letters* **4**, 1349-1355 (2019).

30 Burns, J. *et al.* Predicting and extending the lifetime of Li-ion batteries. *Journal of The Electrochemical Society* **160**, A1451 (2013).

31 Xu, S., Chen, K.-H., Dasgupta, N. P., Siegel, J. B. & Stefanopoulou, A. G. Evolution of Dead Lithium Growth in Lithium Metal Batteries: Experimentally Validated Model of the Apparent Capacity Loss. *Journal of*

The Electrochemical Society **166**, A3456 (2019).

32 Gao, N. *et al.* Fast Diagnosis of Failure Mechanisms and Lifetime Prediction of Li Metal Batteries. *Small Methods* **5**, 2000807 (2021).

33 Xiao, J. *et al.* Understanding and applying coulombic efficiency in lithium metal batteries. *Nature Energy* **5**, 561-568, doi:10.1038/s41560-020-0648-z (2020).

34 Wood, K. N., Noked, M. & Dasgupta, N. P. Lithium metal anodes: toward an improved understanding of coupled morphological, electrochemical, and mechanical behavior. *ACS Energy Letters* **2**, 664-672 (2017).

35 Wang, L. *et al.* Identifying the components of the solid–electrolyte interphase in Li-ion batteries. *Nat Chem* **11**, 789-796 (2019).

36 Nie, M. *et al.* Lithium ion battery graphite solid electrolyte interphase revealed by microscopy and spectroscopy. *The Journal of Physical Chemistry C* **117**, 1257-1267 (2013).

37 Hirota, N. Electron paramagnetic resonance studies of ion pairs. Structures and equilibria in alkali metal naphthalenide and anthracenide. *Journal of the American Chemical Society* **90**, 3603-3611 (1968).

38 Niu, C. *et al.* High-energy lithium metal pouch cells with limited anode swelling and long stable cycles. *Nature Energy* **4**, 551-559 (2019).

39 Zhang, X. *et al.* Rethinking how external pressure can suppress dendrites in lithium metal batteries. *Journal of The Electrochemical Society* **166**, A3639 (2019).

40 Yin, X. *et al.* Insights into morphological evolution and cycling behaviour of lithium metal anode under mechanical pressure. *Nano Energy* **50**, 659-664 (2018).

41 Louli, A. J. *et al.* Exploring the impact of mechanical pressure on the performance of anode-free lithium metal cells. *Journal of The Electrochemical Society* **166**, A1291 (2019).

42 Monroe, C. & Newman, J. The Impact of Elastic Deformation on Deposition Kinetics at Lithium/Polymer Interfaces. *Journal of The Electrochemical Society* **152**, doi:10.1149/1.1850854 (2005).

43 Liu, F. *et al.* Dynamic spatial progression of isolated lithium during battery operations. *Nature* **600**, 659-663 (2021).

44 Wood, K. N. *et al.* Dendrites and pits: Untangling the complex behavior of lithium metal anodes through operando video microscopy. *ACS central science* **2**, 790-801 (2016).

45 Brissot, C., Rosso, M., Chazalviel, J.-N. & Lascaud, S. Dendritic growth mechanisms in lithium/polymer cells. *Journal of power sources* **81**, 925-929 (1999).

46 Chen, X. R. *et al.* A Diffusion--Reaction Competition Mechanism to Tailor Lithium Deposition for Lithium-Metal Batteries. *Angewandte Chemie* **132**, 7817-7821 (2020).

47 Bai, P., Li, J., Brushett, F. R. & Bazant, M. Z. Transition of lithium growth mechanisms in liquid electrolytes. *Energy Environ. Sci.* **9**, 3221-3229,

doi:10.1039/c6ee01674j (2016).

48 Liu, Y. *et al.* Insight into the Critical Role of Exchange Current Density on Electrodeposition Behavior of Lithium Metal. *Advanced Science* **8**, 2003301 (2021).

49 Yamaki, J.-i. *et al.* A consideration of the morphology of electrochemically deposited lithium in an organic electrolyte. *Journal of Power Sources* **74**, 219-227 (1998).

50 Wang, S. H. *et al.* Stable Li metal anodes via regulating lithium plating/stripping in vertically aligned microchannels. *Advanced Materials* **29**, 1703729 (2017).

51 Chen, B.-R., Kunz, M. R., Tanim, T. R. & Dufek, E. J. A machine learning framework for early detection of lithium plating combining multiple physics-based electrochemical signatures. *Cell Reports Physical Science* **2**, 100352 (2021).

52 Finegan, D. P. *et al.* Spatial dynamics of lithiation and lithium plating during high-rate operation of graphite electrodes. *Energy Environ. Sci.* **13**, 2570-2584 (2020).

Table of Content

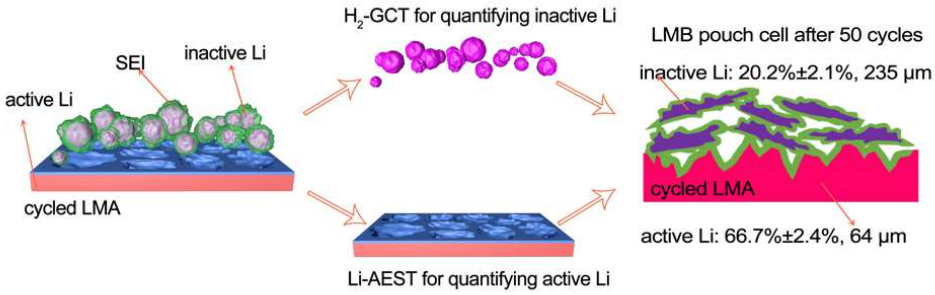

Supplementary Files

This is a list of supplementary files associated with this preprint. Click to download.

- Supplementaryinformation20220128.docx